

Targeted Fe-Doping of Ni–Al Catalysts via the Surface Redox Reaction Technique for Unravelling its Promoter Effect in the CO₂ Methanation Reaction

Thomas Burger,^[a, b] Hannah M. S. Augenstein,^[a, b] Franziska Hnyk,^[a, b] Markus Döblinger,^[c] Klaus Köhler,^[a, b] and Olaf Hinrichsen^{*[a, b]}

In promoted catalyst systems, the location of dopants is of very high interest to investigate promoter effects. A Ni/Al₂O₃ catalyst ($w_{\text{Ni}} = 11$ wt.%) prepared by deposition-precipitation and a co-precipitated NiAlO_x ($n_{\text{Ni}}/n_{\text{Al}} = 1$) catalyst are modified with Fe by means of the surface redox reaction technique and tested for activity under differential and integral conditions and for thermal stability (aging at 500 °C, 8 bar, 32 h) in the methanation reaction of CO₂. By applying detailed material characterization studies comprising H₂ and CO₂ chemisorption, ICP-OES,

XRD, STEM-EDX, FMR and BET, it is shown that the surface deposition techniques can be used to selectively deposit Fe in the vicinity of Ni nanoparticles. Doping with Fe leads to an increase of the catalytic activity, attributed to electronic effects through the formation of surface Ni–Fe alloys, and, for the co-precipitated Ni–Al catalyst, to an enhancement of the apparent thermal stability at higher Fe loadings, which is assumed to be caused by a dynamic variation of Ni, Fe, and Al interactions depending on the reaction conditions.

1. Introduction

The CO₂ methanation reaction has recently gained interest for its role in the power-to-gas concept.^[1] Synthetic natural gas (SNG) can be stored and distributed in the natural gas grid and therefore serve as a chemical energy storage to buffer fluctuations as well as regional and seasonal dependencies of energy supply by renewables.^[2] The highly exothermal character of the CO₂ methanation reaction ($\Delta_{\text{r}}H_{298\text{K}} = 165$ kJ mol⁻¹) leads to a demand for both high catalytic activity to achieve high CH₄ yields at mild operating conditions and high thermal stability to increase catalyst life-time by avoiding excessive catalyst deactivation, e.g. by sintering processes,^[3] in industrial fixed bed application. Due to its high abundance and low costs,^[4] as well as its high selectivity to methane formation,^[2d] Ni^[5] is

preferred over other active metals like Rh,^[6] Pd,^[7] Ru,^[8] Pt or Ir.^[9] Fe has been claimed to enhance the activity of Ni-based catalyst systems by electronic modification of the active Ni centers, forming Ni–Fe alloy particles.^[10] The effect of Fe on kinetics, however, is not conclusively clarified yet. In literature, the associative and the dissociative methanation pathway are controversially discussed.^[11] In associative methanation, CO₂ adsorbs on the catalyst surface on basic sites and undergoes hydrogenation at the interface of the Ni particles, where H_{ads} is supplied.^[5e,12] Therein, catalyst performance is critical to the density and distribution of basic sites.^[12c] In the dissociative mechanism, both H₂ and CO₂ adsorb dissociatively.^[13] In this case, it is generally accepted that C–O bond cleavage is rate-determining.^[14] The reported effects of Fe, however, are manifold. Mebrahtu *et al.* showed that surface basicity can be tuned by varying the Fe loading in NiMgAlO_x catalysts.^[10f] The Nørskov group showed in an Bronsted-Evans-Polyani relation approach that Ni–Fe alloys feature improved C–O dissociation energies, leading to an improved methanation performance.^[15] The computational approach was also transferred to experimental studies^[16] and is in line with our findings for co-precipitated NiFeAlO_x catalysts^[10a,17] and results from Hwang *et al.*, who also claimed that Fe doping to Ni–Al xerogel catalysts decreases the metal-support interactions.^[10e] In addition, beneficial effects of Fe on the reducibility of NiO^[17–18] and the Ni dispersion^[18] were reported.

Besides the positive effect of Fe on the methanation activity, we recently proved an enhancement of the apparent thermal stability under aging conditions for co-precipitated NiFeAlO_x catalysts at sufficiently high Ni/Fe ratios.^[10a] However, the reasons for the stability improvement are not clear yet.

When applying conventional catalyst preparation techniques like impregnation or (co-)precipitation for metal doping, the promoter may be distributed on the catalyst surface or

[a] T. Burger, H. M. S. Augenstein, F. Hnyk, Prof. K. Köhler, Prof. O. Hinrichsen
Department of Chemistry
Technical University of Munich
Lichtenbergstr. 4
Garching b. München 85748 (Germany)
E-mail: olaf.hinrichsen@ch.tum.de

[b] T. Burger, H. M. S. Augenstein, F. Hnyk, Prof. K. Köhler, Prof. O. Hinrichsen
Catalysis Research Center
Technical University of Munich
Ernst-Otto-Fischer-Str. 1
Garching b. München 85748 (Germany)

[c] Dr. M. Döblinger
Department of Chemistry
University of Munich
Butenandstr. 5–13
München 81377 (Germany)

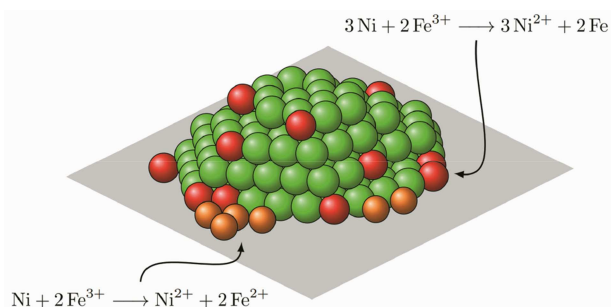
 Supporting information for this article is available on the WWW under <https://doi.org/10.1002/cctc.201901331>

 © 2019 The Authors. Published by Wiley-VCH Verlag GmbH & Co. KGaA. This is an open access article under the terms of the Creative Commons Attribution License, which permits use, distribution and reproduction in any medium, provided the original work is properly cited.

within the catalyst structure, and the location of the promoter relative to the active metal centers is usually unknown. In addition, for its redox properties especially true for Fe, the promoter may be present in different oxidation states (depending on its location), complicating conclusive decisions on its effect and structure-activity relationships. Therefore, this work addresses the investigation of the promoting effect of Fe on Ni–Al catalysts selectively doped at the Ni centers by means of the surface redox reaction (SRR) method to better understand the effect of Fe on Ni–Al catalysts in the CO₂ methanation reaction exclusively on the Ni centers.

The surface redox reaction (SRR) method is a known material preparation procedure,^[19] but rather rarely used and, to the best of our knowledge, has not been applied to Ni–Fe–Al systems in the CO₂ methanation so far. It can be applied to selectively replace metal atoms on a material by atoms of a different metal with a lower reduction potential in an appropriate solvent. In this work, Fe³⁺ ions dissolved in EtOH are used to oxidize Ni atoms on the activated NiAlO_x catalyst. Scheme 1 illustrates the reactions possible on a Ni particle under the chosen conditions. The Fe species are deposited at the location where the electrons are supplied in the form of Fe⁰ or Fe²⁺, or maintain in solution as Fe²⁺, while the generated Ni²⁺ ions go into solution. The synthesis procedure is very sensitive to the washing process after the surface redox reaction to avoid any formation of clusters of the oxidizing or oxidized ion species by adsorption from the liquid phase or by impregnation during the drying process. Therefore, these catalyst synthesis steps were investigated and reported very detailed in this paper.

A Ni/Al₂O₃ catalyst prepared by deposition-precipitation and a co-precipitated NiAlO_x catalyst were taken as the template catalysts for the surface redox reaction. Besides the approach of doping Fe in a selective manner to the Ni nanoparticles, the comparison of the impact of Fe on two differently synthesized Ni–Al template catalysts that vary in structure and sorption properties may shine some light on the importance of particle-support interactions and morphology on the promoter effect of Fe. The Ni loading of the precipitated Ni/Al₂O₃ catalyst was set to a typical value of 11 wt.%. For the co-precipitated benchmark catalyst, the molar Ni/Al ratio was set to one to provide data comparable to previous studies.^[10a] The catalysts are



Scheme 1. Doping of an activated Ni–Al catalyst with Fe by means of the surface redox reaction, green: Ni, red: Fe, orange: Fe²⁺, grey: oxidic Al-rich phase.

labelled Ni_yFe_zZ, where Y and Z, respectively, denote the metal loadings, subscript x indicates that the catalyst was derived from the co-precipitated NiAlO_x catalyst.

2. Results and Discussion

2.1. Evaluation of Fe Deposition During the Surface Redox Reaction

The metal loadings and the molar element ratios of the catalysts prepared from the template catalysts are listed in Table 1.

For all SRR-modified catalysts, the amount of the Fe precursor substance Fe(NO₃)₃·9 H₂O used during synthesis (*cf.* Table 3) correlates well with the Fe loading on the catalyst. At the same time, a decrease of the Ni loading is observed, owed to the exchange of Ni with Fe. The catalysts originating from the co-precipitated NiAlO_x catalyst feature molar Ni/Fe ratios of 9.3, 5.7, and 3.0, respectively, making them comparable to our recent study on co-precipitated NiFeAlO_x catalyst.^[10a]

The exchange ratio $\Delta N_{\text{Fe}}/\Delta N_{\text{Ni}}$ describes the number of Fe atoms that are deposited on the catalyst per removed Ni atom. As depicted in Scheme 1, two competing reaction mechanisms need to be considered: Fe³⁺ may either be reduced to Fe⁰ ($\Delta N_{\text{Fe}}/\Delta N_{\text{Ni}}=2/3$), which is deposited on top or the perimeter of the Ni particle, or to Fe²⁺, which may either be deposited on perimeter sites ($\Delta N_{\text{Fe}}/\Delta N_{\text{Ni}}=2$), or stay in solution. The latter pathway seems to be the prominent one in our approach, since, for all catalysts, $\Delta N_{\text{Fe}}/\Delta N_{\text{Ni}}$ is lower than the expected minimum value of 2/3. This also indicates that a considerable amount of Fe³⁺ is reduced to Fe²⁺, remaining in solution rather than being deposited on the surface. In agreement, the presence of Fe²⁺ in the solution was experimentally qualitatively proven by Turnbull's blue formation after adding [Fe(CN)₆]³⁻ (Merck, *p.a.*). The molar amount of Al in the samples stays constant in all catalysts, no Al³⁺ leaching in EtOH could be observed by ICP-OES. Suspending the samples in H₂O, in contrast, led to significant leaching of Al³⁺ as well as γ -AlO(OH) formation (proven by XRD, not shown) for experiment times exceeding 24 h, which is consistent to processes occurring during hydrothermal treatments, however, reported in literature.^[20] Therefore, the washing times after the SRR treatment in H₂O were kept as short as 2 min. Washing the catalysts five times in fresh

Table 1. Metal loadings and elemental ratios determined by ICP-OES.

Catalyst	w_{Ni} (wt.%)	w_{Fe} (wt.%)	$n_{\text{Ni}}/n_{\text{Fe}}$	$n_{\text{Ni}}/n_{\text{Al}}$	$n_{\text{Fe}}/n_{\text{Al}}$	$\Delta N_{\text{Fe}}/\Delta N_{\text{Ni}}$
Precipitated template catalyst Ni/Al ₂ O ₃						
Ni11–EtOH	11.0	–	–	0.114	–	–
Ni9Fe0.5	8.7	0.5	17.2	0.095	0.006	0.31
Ni7Fe1	6.6	1.0	6.0	0.073	0.012	0.31
Ni5Fe2	5.3	1.8	2.8	0.054	0.019	0.32
Co-precipitated template catalyst NiAlO _x						
Ni48 _x –EtOH	48.1	–	–	1.04	–	–
Ni39 _x Fe4	38.7	3.6	10.3	0.84	0.08	0.39
Ni36 _x Fe6	36.4	6.1	5.7	0.74	0.13	0.42
Ni27 _x Fe9	27.5	8.6	3.0	0.58	0.19	0.41

Table 2. Material characterization data and activation energies, determined before (1) and after aging (2).

Catalyst	S_{Ni} ($\text{m}^2\text{g}_{\text{cat}}^{-1}$)		$d_c^{[a]}$ (nm)		$U(\text{CO}_2)$ ($\mu\text{mol g}_{\text{cat}}^{-1}$)		S_{BET} ($\text{m}^2\text{g}_{\text{cat}}^{-1}$)		V_p ($\text{ml g}_{\text{cat}}^{-1}$)		d_p (nm)		E_A (kJ mol^{-1})	
	1	2	1	2	1	2	1	2	1	2	1	2	1	2
Precipitated template catalyst Ni/Al ₂ O ₃														
Ni11-EtOH	7.7	1.9	5.2	6.4	230	119	182	146	0.40	0.39	7.7	10.9	72.5 ± 0.6	73.1 ± 0.2
Ni9Fe0.5	7.3	1.8	4.8	5.4	228	129	186	149	0.41	0.39	7.8	10.9	74.5 ± 0.5	75.4 ± 0.3
Ni7Fe1	5.2	1.6	4.5	5.2	227	135	192	145	0.41	0.42	7.8	10.9	76.9 ± 1.9	76.5 ± 1.0
Ni5Fe2	2.3	0.9	4.4	5.5	234	132	199	146	0.44	0.41	8.6	10.9	84.0 ± 3.1	80.2 ± 1.1
Co-precipitated template catalyst NiAlO _x														
Ni48 _x -EtOH	42.5	18.6	3.4	4.2	261	129	263	127	-	-	-	-	75.7 ± 0.6	76.3 ± 1.0
Ni39 _x Fe4	25.9	11.2	3.4	4.5	255	123	300	129	-	-	-	-	81.6 ± 0.5	81.6 ± 1.8
Ni36 _x Fe6	22.2	10.5	3.9	4.5	220	126	300	127	-	-	-	-	85.6 ± 0.8	89.7 ± 1.5
Ni27 _x Fe9	8.2	6.2	4.1	4.4	167	122	300	123	-	-	-	-	89.7 ± 1.4	97.1 ± 0.3

1 before aging. 2 after aging. [a] Determined from the Ni, (yFe,Ni) diffraction peak at $2\theta = 51.5\text{--}51.8^\circ$.

Table 3. Catalyst and precursor masses, and solvent volumes used during the surface redox reaction.

Catalyst	m (catalyst) [g]	m (Fe(NO ₃) ₃ ·9 H ₂ O) [g]	V (EtOH) [ml]
Precipitated template catalyst Ni/Al ₂ O ₃			
Ni11-EtOH	1.0	-	25
Ni9Fe0.5	0.83	0.13	25
Ni7Fe1	0.83	0.81	25
Ni5Fe2	0.83	1.5	25
Co-precipitated template catalyst NiAlO _x			
Ni48 _x -EtOH	1.0	-	20
Ni39 _x Fe4	1.0	3.8	20
Ni36 _x Fe6	1.0	6.1	20
Ni27 _x Fe9	1.0	8.6	20

degassed water, however, proved to be crucial to wash away redundant Fe^{*n*+} (*n* = 2,3) and Ni²⁺ species from the liquid phase, and to re-dissolve clusters nucleated on the Al-containing oxide surface. The Fe and Ni contents in the fifth washing filtrate were checked to be below 0.05 mg g_{cat}⁻¹ by ICP-OES, highlighting that both the amount of Fe species being adsorbed on the surface and the amount of Ni and Fe being re-impregnated on the catalyst surface during drying can be neglected. Besides, the combination of this washing procedure and the degassing at 250 °C ensured that no remaining C species originating from EtOH remained on the catalyst, as checked by BET and CHN analysis in pre-studies.

The constant exchange ratios of $\Delta N_{\text{Fe}}/\Delta N_{\text{Ni}}$ (0.31 to 0.32) for the catalysts originating from the precipitated Ni/Al₂O₃ template catalyst and 0.39 to 0.42 for the co-precipitated NiAlO_x template catalyst prove that the doping process via the SRR technique is reproducible. The offset of about 0.1 between the template catalysts may result from the differences in the Ni particle size (e.g. accessible Ni sites) and morphological properties.

2.2. Scanning Transmission Electron Microscopy/Energy Dispersive X-ray Spectroscopy

Due to their strong ferromagnetic character after reduction (compare also chapter on FMR studies), no STEM images or EDX data of the activated or aged catalyst samples could be collected. The local atomic distributions of Ni, Fe and Al in

calcined Ni5Fe2, resolved by STEM-EDX, are exemplarily shown in Figure SI 2, local intensity distributions of Ni-K_α, Al-K_α and Fe-K_α in Figure 1A. As expected for a classical supported Ni/Al₂O₃ catalyst, clear NiO clusters in the range of 6 nm can be observed. Fe is not statistically distributed on the surface, but rather located on concentrated spots in close neighborhood to Ni-rich sites (cf. Figure 1A). On the Fe-rich spots, the Ni signal is reduced (e.g. Figure SI 2B, Area 1), consistent with the replacement mechanism proposed in Scheme 1.

As apparent from Figure 1B and Figure SI 3, on Ni27_xFe9, in contrast, Ni and Al are more homogeneously distributed. The central areas in Figure SI 3 A and SI 3 B feature a very homogenous distribution of both Al and Ni. No distinct NiO clusters can be observed, which highlights the different morphologies of a supported Ni/Al₂O₃ catalyst and a co-precipitated NiAlO_x catalyst. Moreover, Figure SI 3C indicates that different phases exist, one rich in Ni²⁺ and one that is rich

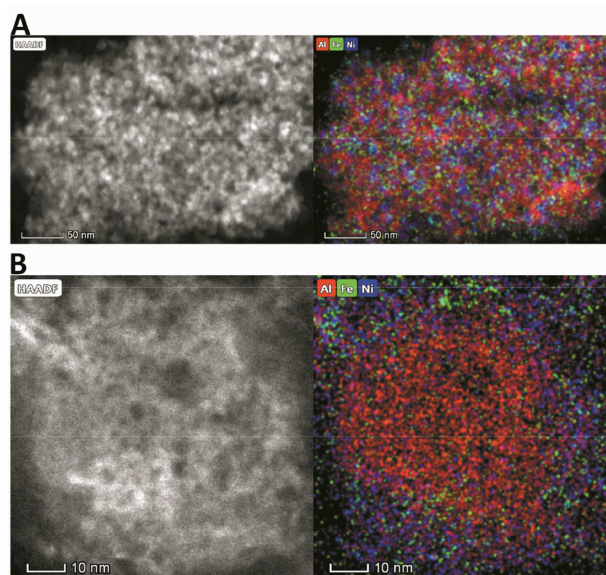


Figure 1. HAADF-STEM image and local EDX intensity distribution of Ni-K_α (blue), Al-K_α (red), and Fe-K_α (green) in the Ni5Fe2 (A) and Ni27_xFe9 (B) catalysts in their calcined (oxidized) state.

in Al^{3+} and poor in Ni^{2+} . Fe, again, seems to be co-localized rather with Ni^{2+} than with Al^{3+} . Elemental analysis data (by EDX) of selected spots in Figure 1 are shown in the ESI.

Based on the STEM-EDX observations on the Ni_5Fe_2 and $\text{Ni}_{27}\text{Fe}_9$ samples and on the strong correlation of $\Delta N_{\text{Fe}}/\Delta N_{\text{Ni}}$, one can conclude that the replacement mechanism proposed in Scheme 1 is valid.

2.3. Structural Characterization

The co-precipitated NiAlO_x template catalyst features a hydroxalcite structure after co-precipitation. The structural and morphological properties of this takovite-like co-precipitated $[\text{Ni}_{0.5}\text{Al}_{0.5}(\text{OH})_2(\text{CO}_3)_{0.25} \cdot n \text{H}_2\text{O}]$ material have been extensively discussed in previous studies^[10a,17,21] and therefore are not repeated in this work.

Figure 2 shows the XRD patterns of the calcined Ni–Al catalysts prior to the SRR treatment. For the calcined $\text{Ni}/\text{Al}_2\text{O}_3$, the characteristic $\gamma\text{-Al}_2\text{O}_3$ reflections appear at $2\theta = 37.6^\circ$, 39.5° , 45.9° and 67.0° (JCPDS 10-0475), the NiO reflections at $2\theta = 37.3^\circ$, 43.3° , 61.9° , 75.4° , and 79.4° (JCPDS 78-4029). The presence of these two crystalline phases in the precipitated catalyst is typical for a classical supported catalyst, where NiO clusters are dispersed on the Al_2O_3 support, in accordance to STEM-EDX. In contrast, for the co-precipitated NiAlO_x catalyst, the reflections attributed to NiO are shifted towards the respective peaks of $\gamma\text{-Al}_2\text{O}_3$, which indicates that Al^{3+} is incorporated into the NiO crystal lattice, leading to lattice shrinkage ($2\theta = 36.9^\circ$, 44.1° , 63.9° , 76.2° , and 81.0°).

Besides the obvious presence of this crystalline NiO-rich phase, Alzamora *et al.* proposed the co-existence of a second X-ray amorphous Al-rich Ni-containing alumina-like phase,^[22] which is consistent to the previously discussed observations from STEM-EDX in Figure SI 3. This structure is common to hydroxalcite-derived materials^[22–23] and greatly varies from the one of the precipitated $\text{Ni}/\text{Al}_2\text{O}_3$ catalyst. Noteworthy, no bulk

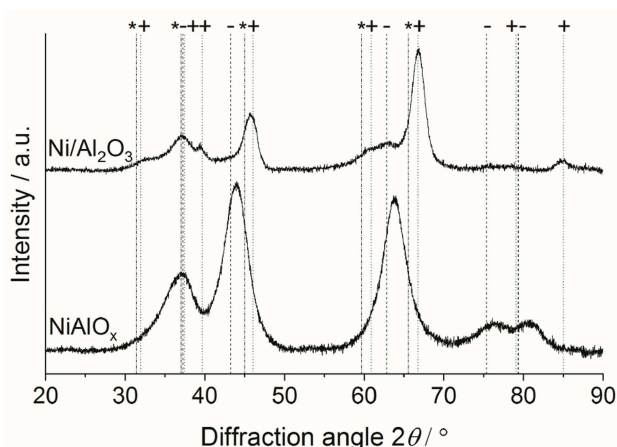


Figure 2. XRD patterns of the $\text{Ni}/\text{Al}_2\text{O}_3$ and the NiAlO_x catalyst after calcination, – NiO (JCPDS 78-4029), + $\gamma\text{-Al}_2\text{O}_3$ (JCPDS 10-0475), * NiAl_2O_4 (JCPDS 10-0339).

NiAl_2O_4 spinel phase can be found by XRD for any of the catalysts.

The XRD patterns of the reduced reference catalysts $\text{Ni}_{11}\text{-EtOH}$ and $\text{Ni}_{48}\text{-EtOH}$ are shown in Figure 3. The characteristic fcc Ni peaks evolve at $2\theta = 44.50^\circ$, 51.85° , and 76.38° . From the Scherrer equation, the Ni crystallite sizes can be estimated to be 6.1 nm for $\text{Ni}/\text{Al}_2\text{O}_3\text{-EtOH}$ and 3.4 nm for $\text{Ni}_{48}\text{-EtOH}$. It needs to be mentioned that this low particle diameter for the co-precipitated catalyst is close to the application limit of the Scherrer equation, but nevertheless is consistent with particle size distributions obtained by transmission electron microscopy studies in literature.^[2b,24]

The catalyst samples are not reduced quantitatively. While the remaining NiO species seem to be X-ray amorphous or too little to be detected by XRD for $\text{Ni}_{11}\text{-EtOH}$ in Figure 3A, their

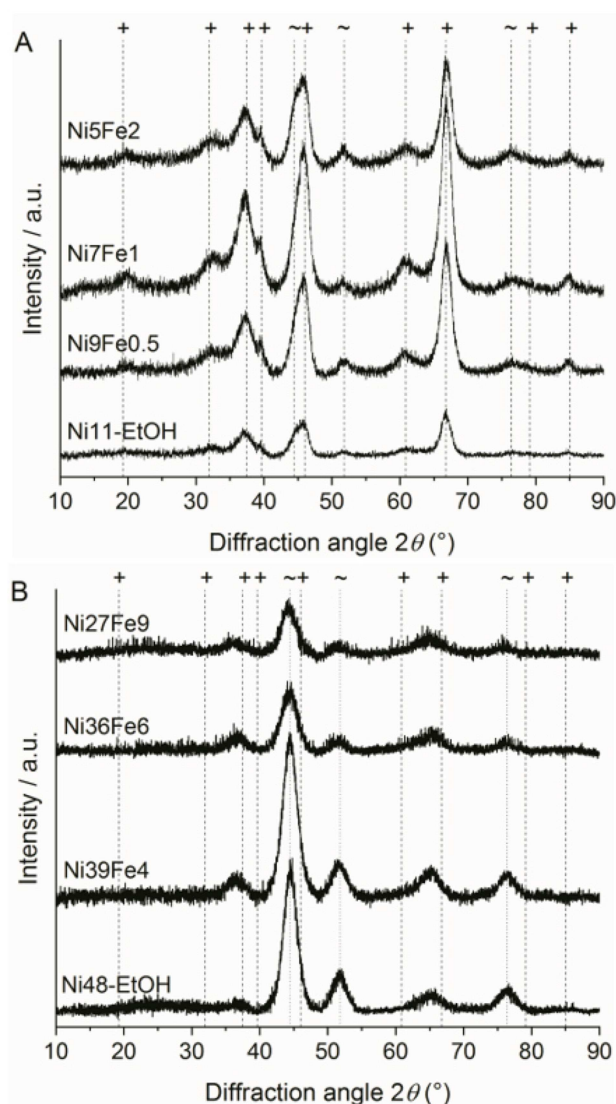


Figure 3. XRD patterns of the $\text{Ni}_{11}\text{-EtOH}$ reference catalyst as well as the $\text{Ni}/\text{Al}_2\text{O}_3$ -derived Fe-doped catalyst samples after activation (A) and the $\text{Ni}_{48}\text{-EtOH}$ reference catalyst as well as the NiAlO_x -derived Fe-doped catalyst samples after activation (B), + $\gamma\text{-Al}_2\text{O}_3$ (JCPDS 10-0475), ~ Ni, (ICCD 96-901-3002).

presence in Ni_{48-x}-EtOH is still evident from Figure 3B. Albeit the reflections caused by the NiO-rich mixed oxide shift towards alumina during reduction (*cf.* Figure 3B, reflections at 36° and 66°), which indicates the partial removal of Ni²⁺ during catalyst activation, some Ni²⁺ remains in this freshly formed crystalline Al³⁺-rich oxide phase, since its changed reflection signal still does not meet the reflection positions of γ -Al₂O₃.

For all Fe-promoted samples, no distinct reflexes caused by Fe species can be observed in the XRD patterns. However, with increasing Fe loading, for both the catalysts derived from the Ni/Al₂O₃ (*cf.* Figure 3A) and the NiAlO_x (*cf.* Figure 3B) template catalysts, shifts of the 111, 200, and 220 fcc Ni reflexes to lower diffraction angles can be observed. The corresponding increase of the lattice constant *a* can be explained by the insertion of Fe atoms into the crystal lattice of fcc Ni, effectively leading to the formation of (γ -Fe,Ni) alloy particles.^[25] The bulk composition of the alloy particles can be estimated by line profiling and comparison to tabulated values.^[26] From the step width, an absolute error of 0.7 at.% can be assumed for *x*_{Fe}, detailed data is given in Table SI 1. While for Ni₉Fe_{0.5} the bulk of the particles only contains 2.5 at.% Fe, the Fe content stepwise increases to 4 at.% for Ni₇Fe₁ and 8 at.% for Ni₅Fe₂. Comparison to the overall Ni/Fe molar ratios in the catalyst (*cf.* Table 1) shows that the Ni/Fe molar ratio in the bulk alloy particles is significantly higher, which suggests that the majority of Fe atoms is located on the outer surface in vicinity to or on top of the Ni-rich (γ -Fe,Ni) particles, in the form of a Ni-Fe surface alloy or Fe²⁺, not contributing to the alloy formation in the bulk of the particles.

A similar picture is found for the catalysts derived from the NiAlO_x template catalyst. However, the degree of bulk alloying is significantly higher. For Ni₃₉Fe₄, the bulk of the (γ -Fe,Ni) particles contains 11 at.% Fe, which further increases to 15.5 at.% for Ni₃₆Fe₆ to 21 at.% for Ni₂₇Fe₉. The molar Ni/Fe ratios in the particles are much closer to the overall molar Ni/Fe ratios listed in Table 1.

These observations suggest that for the NiAlO_x-derived (co-precipitated) catalysts Ni-Fe alloy formation under reductive conditions (500 °C, H₂) seems to be preferred compared to Ni/Al₂O₃-derived (precipitated) catalysts, which might be caused by particle size effects or different stabilization of the particles on the oxidic phases.

2.4. Paramagnetic and Ferromagnetic Resonance Spectroscopy

A further indicator for the composition of the metal particles on the reduced catalysts is the change of the magnetic properties resolved by ferromagnetic resonance spectroscopy (FMR). All activated (reduced) catalyst samples show spectra, line intensities and thermomagnetic behavior typical for ferromagnetic particles, but with varying parameters for the different iron contents.

These differences in the magnetizations (*I*_{rel}), ΔB_{pp} , shift of *g*-values or anisotropy of the FMR spectra are described in the

literature by variations of the Ni particle size and interactions with the support or adsorbed molecules.^[27]

Ni₁₁-EtOH (*cf.* Figure SI 4A) features a significantly higher anisotropy (at *T* = 133 K) of the FMR spectrum compared to Ni_{48-x}-EtOH (*cf.* Figure SI 5A). For Ni₅Fe₂ (*cf.* Figure SI 4B), a severe impact of Fe can be observed. The anisotropy of the FMR spectrum, evident from the decrease of ΔB_{pp} (at 133 K, *cf.* Figure SI 4C) is significantly reduced, while the magnetization (*I*_{rel}) increases. This behavior can be explained by the interference of the ferromagnetic characteristics of Ni and metallic Fe, possibly by Fe atoms located on the surface of Ni particles.

The drastic changes of the ferromagnetic characteristics between the activated Ni_{48-x}-EtOH (*cf.* Figure SI 4A) and Ni₂₇Fe₉ (*cf.* Figure SI 5B) are absolutely analogous to the co-precipitated Ni-Fe-Al catalyst^[10a] and can only be explained by a substantial ferromagnetic contribution of metallic Fe and the assumption of the formation of Ni-Fe alloy particles. This is reflected by the strong increase of all relevant criteria as anisotropy of the FMR spectra and Δg , of magnetization (*I*_{rel}), and ΔB_{pp} (at 133 K, *cf.* Figure SI 5C) for Ni₂₇Fe₉ and is reported in detail in^[10a] (and literature cited therein) and in the SI.

2.5. Catalyst Reducibility

Figure 4A illustrates the TPR profiles for the Ni/Al₂O₃-derived catalysts, Figure 4B the ones of the NiAlO_x-derived catalysts. For Ni/Al₂O₃, a broad asymmetric reduction signal ranging from 360 to 760 °C, caused by two overlapping reduction peaks centered at 520 and 615 °C, respectively, and a shoulder at 780 °C can be observed. The peak at 520 °C can be attributed to the reduction of Ni²⁺ weakly interacting with γ -Al₂O₃, while the peak centered at 615 °C is supposed to be caused by the reduction of Ni²⁺ that more strongly interacts with γ -Al₂O₃.^[28] The third, high-temperature peak at 780 °C indicates the presence of Ni²⁺ possibly captured in a spinel-like structure.^[29] Thereby, the presence of such Ni²⁺ species seems to be limited to the catalyst surface, as significant amounts of bulk spinel formation can be excluded on the basis of XRD shown in Figure 2. The NiAlO_x template catalyst features three reduction signals. The small low temperature signal at *T* = 150 °C has previously been assigned to Ni³⁺ in the outer layers of the catalyst structure.^[25] In addition, two overlapping high temperature signals can be observed. The larger reduction signal centered at 585 °C originates from the reduction of Al³⁺-containing NiO, while the smaller signal at higher temperature (680 °C) is caused by the reduction of Ni²⁺ incorporated in the Al³⁺-rich oxide phase.^[30]

For all Fe-doped catalysts, clear signals that can be assigned to the stepwise reduction of Fe³⁺ to Fe can be found. This suggests that the SRR-modified catalysts get re-oxidized in the degassing step by NO₃⁻, that probably forms the counter ion of Fe²⁺ species located near the perimeter of the Ni(Fe) particles, but also indicates the presence of metallic Fe on the catalysts after reduction at 500 °C.

The reduction of Fe³⁺ on the Fe-promoted Ni/Al₂O₃-derived catalysts occurs in the temperature range between 250 to 500 °C. The first peak centered at 330 °C corresponds to the

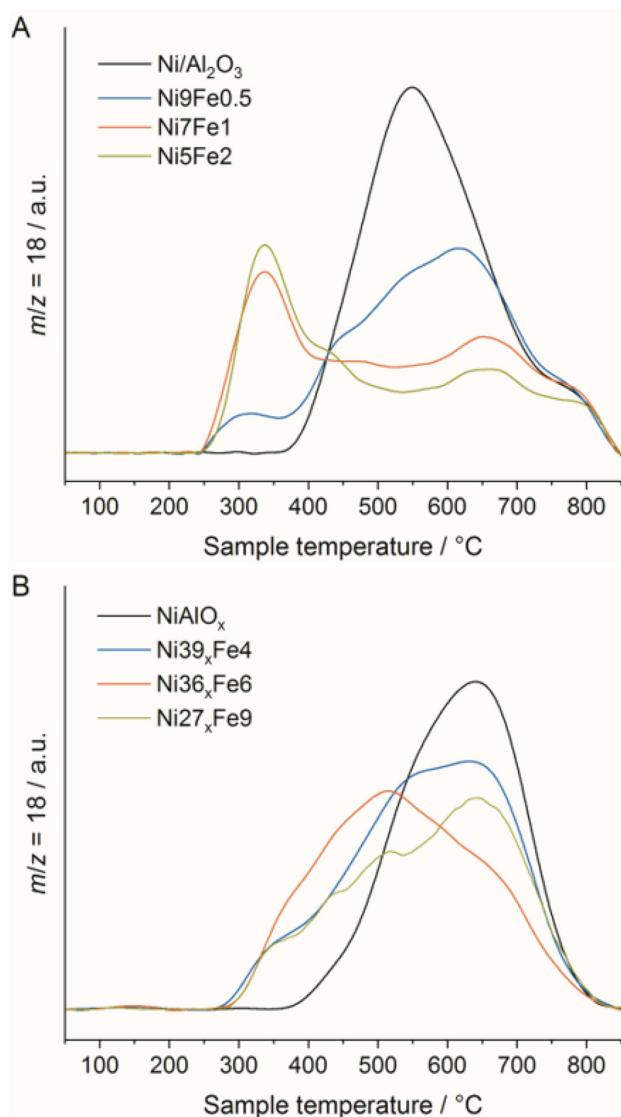


Figure 4. TPR profiles of the Ni/Al₂O₃ template catalyst as well as the Ni/Al₂O₃-derived Fe-doped catalyst samples (A) and the NiAlO_x template catalyst as well as the NiAlO_x-derived Fe-doped catalyst samples (B).

reduction of Fe³⁺ to Fe²⁺, the shoulder at 420 °C marks the reduction of Fe²⁺ to Fe⁰. The reduction signals of Fe are superimposed by the three reduction signals of NiO previously discussed and increase with increasing Fe loading.

Similar observations can be made for the Fe-doped NiAlO_x-derived catalysts. The shoulders at 350 and 410 °C can be attributed to the reduction of Fe³⁺ and Fe²⁺, respectively. The reduction peaks, however, are further superimposed by the reduction of Ni²⁺ from the Ni-rich Ni–Al mixed oxide, that is shifted to lower temperature with decreasing Ni loading. The decrease of the reduction signal from Ni₃₆Fe₆ to Ni₂₇Fe₉ is caused by the decrease in Ni loading, superimposing the reduction signal of Fe³⁺.

2.6. Catalyst Sorption Properties

2.6.1. N₂ Physisorption

The catalysts derived from the precipitated Ni/Al₂O₃ template catalysts feature type VI N₂ adsorption isotherms with H₂ hysteresis loops. The BET surface area of the reference catalyst Ni/Al₂O₃–EtOH amounts to 182 m²g_{cat}^{−1} for the Ni₁₁–EtOH reference catalyst. With increasing iron content, the BET surface area stepwise increases to a maximum of 198 m²g_{cat}^{−1} for Ni₅Fe₂ (cf. Table 2, index 1: before aging). The pore diameter first stays constant at 7.8 nm, but increases to 8.6 nm for Ni₅Fe₂. At the same time, for Ni₅Fe₂ a slightly increased pore volume (0.43 mlg_{cat}^{−1} compared to 0.39 to 0.40 mlg_{cat}^{−1}) is observed. Despite the approach of a mild drying process (cf. Experimental), this increase in porosity can be attributed to the rapid evolution of NO_x during degassing after the surface redox reaction inside the pores, which may lead to further pore formation or rupture of small pores. The amount of NO_x released during the degassing step (which is proportional to the Fe loading) can be correlated to the increase of the BET surface area and the pore volume.

The BET surface areas of the hydrotalcite-derived catalysts are significantly higher. For the reference Ni₄₈–EtOH catalyst, a BET surface area of 263 m²g_{cat}^{−1} is obtained. For all Fe-modified catalysts, the BET surface area stays constant at 300 m²g_{cat}^{−1}. The lower BET surface area of Ni₄₈–EtOH can be explained by the difference in the processes occurring during the thermal pre-treatments. While the Fe-modified catalyst samples are re-oxidized during the degassing by NO₂ as stated above, Ni₄₈–EtOH stays in its reduced state. In the second reduction treatment, Ni₄₈–EtOH seems to undergo some aging, leading to a decrease of the specific BET surface area. For the Fe-modified catalysts, in contrast, the mixed oxide phase is reconstructed during oxidation, and re-reduction leads to a similar BET surface area as obtained after the first reduction step. In accordance to this hypothesis, the specific BET surface area of the template NiAlO_x catalyst after the first reduction amounts to 300 m²g^{−1}. This indicates that (a) Fe does not have an influence on the structural characteristics of the oxidic phase after catalyst activation and that (b), within the investigated range, the Ni/Al ratio, which decreases with increasing Fe loading from Ni₄₈–EtOH to Ni₂₇Fe₉ according to Table 1, does not have a significant impact on the porosity and the characteristics of the oxidic phase after reduction.

In summary, the results from material characterization are in line with the proposed pathway for the surface redox reaction and support the hypothesis that, after catalyst activation, the Fe species interact with the Ni particles rather than with the oxidic phase.

2.6.2. H₂ Chemisorption

For H₂ chemisorption the metal surface area is set equal to the Ni surface area (cf. Table 2, index 1: before aging), since H₂ adsorption on Fe can be neglected under the chosen

conditions.^[25,31] H₂ adsorption at a recommended temperature of 200 °C to account for exposed Fe atoms,^[32] however, resulted in significant H₂ spill-over, making the determination of the metal surface area impossible. Moreover, CO chemisorption could not be applied, since the adsorption stoichiometry of CO on Fe is known to be structure-dependent^[32–33] and therefore is a priori unknown.

For Ni₁₁–EtOH, a Ni surface area of 7.7 m²g_{cat}^{–1} is found. With increasing Fe loading, the Ni surface area decreases, reaching a minimum of 2.3 m²g_{cat}^{–1} for Ni₅Fe₂. This trend is consistent with the NiAlO_x-derived catalyst samples. The very high Ni surface area of Ni_{48_x}–EtOH (*S*_{Ni} = 42.5 m²g_{cat}^{–1}) strongly decreases with the introduction of Fe as a function of Fe loading. Ni_{27_x}Fe₉ features a Ni surface area of 8.2 m²g_{cat}^{–1}.

Based on this trend, three major conclusions can be drawn: first, the samples prepared from the co-precipitated NiAlO_x template catalyst show much higher Ni surface areas compared to the classical supported Ni/Al₂O₃-based catalysts, which has its reason in the unique characteristics of the hydrotalcite-derived oxide, leading to the stabilization of small Ni particles even at high Ni loadings.^[24] Second, with increasing Fe loading, also the amount of Fe species exposed on the surface, blocking H₂ adsorption sites on Ni, is likely to increase for each template catalyst. This trend in the H₂ adsorption capacity is a typical feature for Ni–Fe alloy particles^[25] and therefore consistent with the presence of (γ-Fe,Ni) nanoparticles supported by XRD and FMR. Analogous findings were made for co-precipitated Ni–Fe–Al catalysts for a Ni/Fe ratio > 6.^[10a,17]

Finally, the effect of Fe on the Ni surface area is consistent with the assumption that the Fe atoms were deposited in the neighborhood of the Ni sites during the surface redox reaction.

2.6.3. CO₂ Chemisorption and Temperature-Programmed Desorption

The surface basicity of the catalyst materials as well as the CO₂ binding strength are important parameters in catalyst development for the activation of CO₂. Especially medium basic sites were proposed to play an important role in CO₂ processing under the assumption of an associative CO₂ methanation pathway via hydrogenation of CO₂ adsorbed on the support material at the particle-support interphase.^[12c] In this study, the overall CO₂ uptake of the catalysts is determined by static CO₂ chemisorption, while the binding strength and basic site distribution is investigated by CO₂-TPD. We would like to mention that the total CO₂ uptake does not completely match the uptake determined by CO₂-TPD, since some of the weakly adsorbed CO₂, which is accounted for in static chemisorption experiments, is already removed during the initial purging step prior to the TPD.

As shown in Table 2, the total CO₂ uptake for the catalysts derived from Ni/Al₂O₃ is approx. 230 μmol g_{cat}^{–1}, independent from the Fe loading. Since the total CO₂ uptake primarily mirrors the CO₂ adsorbed basic sites of the oxidic phase, this is a hint that Fe species do not modify the surface basicity of the

Al₂O₃ support, but rather interact with the Ni particles in accordance to XRD, FMR and H₂ chemisorption.

Figure 5A illustrates the corresponding temperature-programmed desorption patterns for the Ni/Al₂O₃-derived catalysts. Four CO₂ desorption signals can be distinguished: CO₂ bound to weak basic sites (peak centered at 90 °C), CO₂ bound to medium basic sites as bidentate carbonate (maximum desorption peak at 150 °C) and monodentate carbonate (desorption peak at 225 °C) as well as CO₂ adsorbed on strong basic sites in the form of “organic-like” carbonates with the maximum desorption signal at 320 °C.^[17,34] The disturbed desorption signal at 390 to 410 °C stems from a negative contribution of CO₂ oxidizing the surface of the metal particles, leading to CO formation.

Within the error range, the TPD patterns of the Fe-doped Ni/Al₂O₃-derived catalysts are very similar, which is especially true for the distribution of basic sites. The majority of CO₂ is bound as bicarbonate on weak basic sites. With decreasing Ni loading, the density of monodentate carbonate sites slightly decreases. The formation of these basic sites is known to be

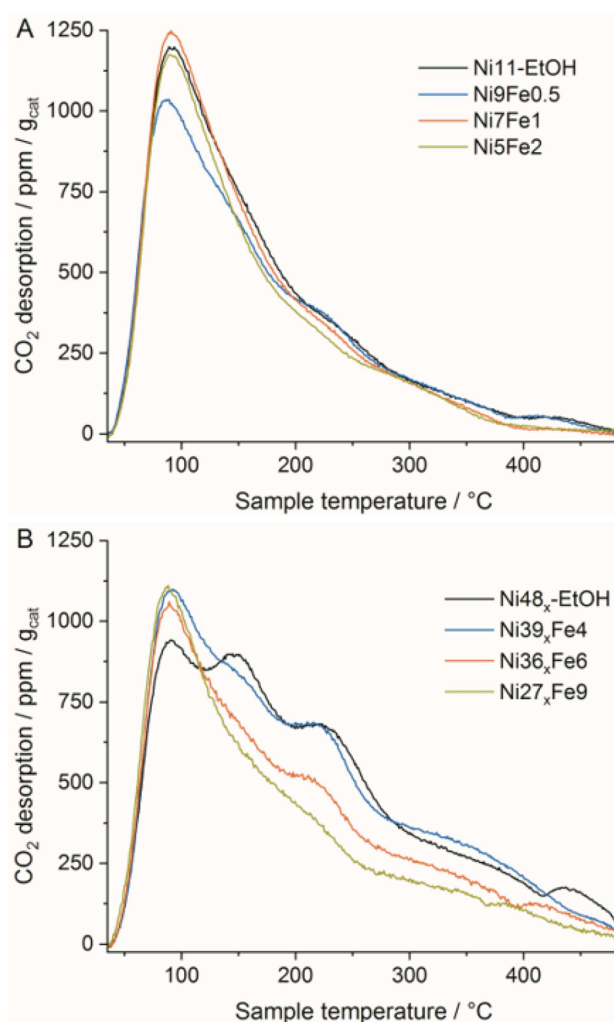


Figure 5. CO₂-TPD patterns of the Ni₁₁–EtOH reference catalyst as well as the Ni/Al₂O₃-derived Fe-doped catalyst samples (A) and the NiAlO_x-derived Fe-doped catalyst samples (B).

promoted by remaining Ni^{2+} in the catalyst structure.^[35] The declining density of these sites therefore may go hand in hand with the decrease of Ni^{2+} remaining unreduced during catalyst activation with increasing Fe loading due to the surface redox reaction.

The CO_2 adsorption characteristics of the NiAlO_x -derived catalysts depicted in Figure 5B, in contrast, differ significantly. For the reference $\text{Ni}_{48_x}\text{-EtOH}$, the total CO_2 uptake is $261 \mu\text{mol g}_{\text{cat}}^{-1}$. Rising Fe loading and decreasing Ni loading then result in a decrease of the CO_2 uptake, reaching a minimum of $167 \mu\text{mol g}_{\text{cat}}^{-1}$ for $\text{Ni}_{27_x}\text{Fe}_9$. This behavior can be explained from the CO_2 desorption patterns in Figure 5B. For the $\text{Ni}_{48_x}\text{-EtOH}$ reference catalyst, four distinct CO_2 desorption signals can be found. With increasing Fe loading, one can observe a stepwise decrease of the medium and strong basic sites, while the density of weak basic sites increases only slightly. As stated above, Ni^{2+} is known to be responsible for the formation of medium and strong basic sites on AlO_x . With an increasing degree of Ni replacement by the introduction of Fe during the surface redox reaction, the effective Ni/Al ratio in the mixed oxide phase after catalyst activation continuously decreases with rising Fe loading, effectively leading to a lower density of medium and strong basic sites. The binding strength of CO_2 on those sites, however, seems to be unaffected. The decrease of the total CO_2 uptake capacity for the hydrotalcite-derived catalysts therefore can be considered as an artefact from the surface redox reaction and is supposed to be caused by the decreasing Ni/Al ratio rather than a detrimental effect of Fe.

2.6.4. Catalyst Performance

The catalysts were tested for activity by means of their temperature vs. CO_2 conversion characteristics and for their stability under aging conditions by an artificial aging treatment for 32 h at 500°C . For reasons of comparison, the results are discussed in separate paragraphs.

2.6.5. CO_2 Methanation Activity

The activity for CO_2 methanation was determined under integral as well as under differential conditions. Figure 6 illustrates the CO_2 conversion vs. temperature characteristics (S_1) for the catalysts derived from the precipitated $\text{Ni/Al}_2\text{O}_3$ (A) and the co-precipitated NiAlO_x (B). For all catalysts, thermodynamic equilibrium gas composition is achieved at 400°C .

All catalysts exhibited excellent selectivity towards methane formation (cf. Figure S1 7 and S1 8). For the $\text{Ni/Al}_2\text{O}_3$ -based catalysts, the maximum selectivities to C_2H_6 (0.4%), C_3H_8 (0.1%), and CO (2.8%) were found at approx. 50% CO_2 conversion. Due to their higher activity, for the catalysts based on NiAlO_x , the maximum selectivities (also in the CO_2 conversion range from 50 to 60%) were 0.9% towards C_2H_6 , 0.2% towards C_3H_8 and 2.5% towards CO, merely independent from the Fe content of the catalyst.

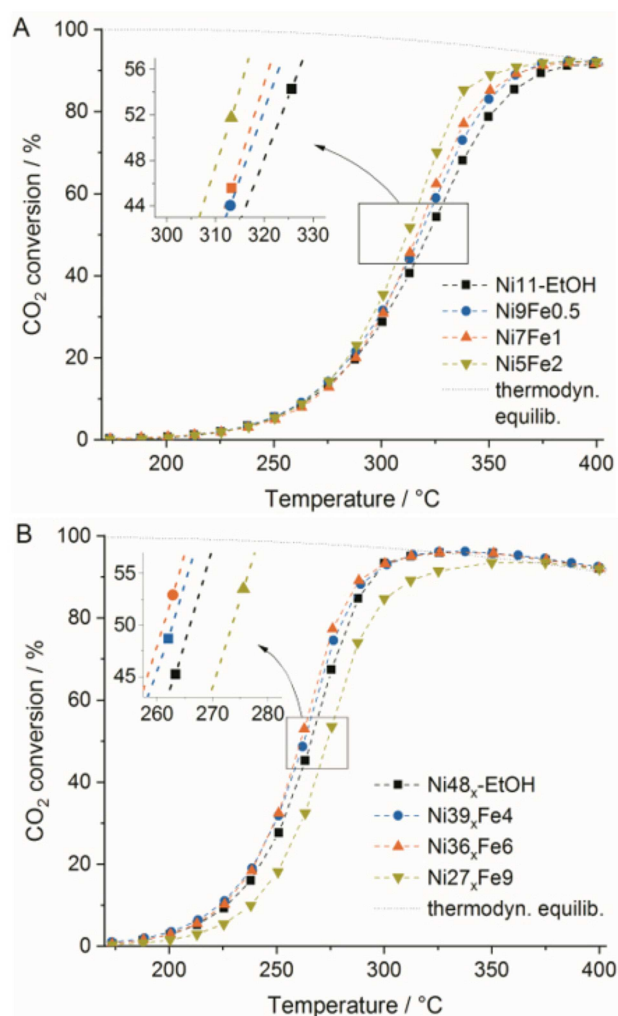


Figure 6. CO_2 conversion vs. temperature plot for the $\text{Ni}_{48_x}\text{-EtOH}$ reference catalyst as well as the $\text{Ni/Al}_2\text{O}_3$ -derived Fe-doped catalyst samples (A) and for the $\text{Ni}_{48_x}\text{-EtOH}$ reference catalyst as well as the NiAlO_x -derived Fe-doped catalyst samples (B).

To compare the activities of the catalysts under integral conditions, the characteristic temperature necessary to obtain a CO_2 conversion of 50% can be evaluated. Based on this consideration, the activity rises in the order $\text{Ni}_{11}\text{-EtOH}$ (321.7°C) < $\text{Ni}_9\text{Fe}_{0.5}$ (320.9°C) < Ni_7Fe_1 (317.5°C) < Ni_5Fe_2 (311.9°C). This order is opposed to the trends of both the Ni loading (cf. Table 1) and the Ni surface area (cf. Table 2). Moreover, since properties like the CO_2 uptake/basic site density and CO_2 binding strength as well as the characteristics of the Al_2O_3 support stay constant, this trend can only be explained by the effect of the Fe promoter on the active sites during CO_2 methanation in accordance to the theory of ($\gamma\text{Fe,Ni}$) nanoparticle formation. Fe may tune the C–O dissociation ability of the active sites, as found in computational analyses based on a Brønsted-Evans-Polanyi approach on the most active nanoparticle step sites by Andersson *et al.* for CO methanation^[15b,36] and CO_2 methanation.^[36] Thereby, it is assumed, in agreement to the general opinion in literature, that the cleavage of the

C–O bond (hydrogen-assisted or via direct C–O dissociation) is the rate-determining step in the methanation reaction.^[2c,14b,15b,36] Their investigations are limited to the assumption of a constant bulk composition of the nanoparticles, which, however, may undergo changes under aging conditions, which is focused on later in this paper.

Interestingly, the behavior under differential conditions suggests a different trend. As shown in Table 2, the apparent activation energy increases with rising Fe loading from 72.5 kJ mol⁻¹ for Ni₁₁–EtOH to 76.9 kJ mol⁻¹ for Ni₇Fe₁ and 84.0 kJ mol⁻¹ for Ni₅Fe₂, which is a clear indicator for the modification of the active sites by the introduction of Fe. The unexpected coupling of a rising activity despite an increasing apparent activation energy can be explained by a distinct compensation effect.^[37] The increase in the apparent activation energy can thereby be caused by an increase of the change of the entropy of the transition complex according to Eyring's theory,^[38] or, more likely, by the simultaneous occurrence of CO₂ methanation on surface centers that involve different activation energies. For the latter case, the determination of the activation energy based on the Arrhenius equation would then yield an average activation energy over all active sites.

The catalytic activities of the NiAlO_x derived catalysts can be explained in a similar manner. The activity under integral conditions rises in the order Ni_{27x}Fe₉ (273.5 °C) < Ni_{48x}–EtOH (265.9 °C) < Ni_{39x}Fe₄ (262.8 °C) < Ni_{36x}Fe₆ (261.2 °C). For Ni_{27x}Fe₉, obviously, the beneficial effect of the Fe promoter can no longer compensate the decrease of the Ni surface area and the CO₂ uptake due to the loss of medium basic sites, which are characteristics that we recently proved to be essential for high methanation activity over co-precipitated catalysts.^[39] This effectively leads to a decrease of catalyst activity. A picture similar to Ni/Al₂O₃ can be drawn when evaluating the activity behavior under differential conditions. Here, the apparent activation energy increases from 75.5 kJ mol⁻¹ for Ni_{48x}–EtOH to 85.6 kJ mol⁻¹ for Ni_{36x}Fe₆ and 89.7 kJ mol⁻¹ for Ni_{27x}Fe₉.

It is noteworthy that, compared to the Ni/Al₂O₃-derived catalysts, the activation energies of the NiAlO_x-derived catalysts for a constant Ni/Fe molar ratio seem to be systematically increased by approx. 4 kJ mol⁻¹, which might have its reason in different characteristics of the nanoparticles depending on the synthesis procedure. Wright *et al.*, for example, showed that in reduced co-precipitated Ni–Al catalysts Al, possibly in the form of (AlO₂)⁻, is incorporated in the nanoparticles, forming a paracrystalline Ni phase,^[40] which might modify the properties compared to crystalline Ni. At this point, we would like to mention that the calculation of TOF values to compare the intrinsic activities of the catalysts was omitted since the number of active sites could not be determined (reasons stated in the experimental section).

2.6.6. Stability of the Catalysts under Aging Conditions

To test the stability of the catalysts under harsh methanation conditions at high temperature and elevated pressure, the catalysts were subjected to an aging treatment in thermodynamic equilibrium at 500 °C, 8 bar for a duration of 32 h. To evaluate the activity after the aging treatment and to resolve data on catalyst stability, thereafter the CO₂ conversion vs. temperature characteristics were recorded again (S2).

Figure 7A–D illustrate the CO₂ conversion vs. temperature characteristics before and after the aging treatment for the catalysts derived from the precipitated Ni/Al₂O₃ catalyst. With increasing Fe loading, the curve recorded after aging is shifted further to higher temperatures. The difference between the characteristic temperatures necessary to obtain a CO₂ conversion of 50%, Δ*T* (X(CO₂) = 50%), can serve as a measure for the apparent stability of the catalyst. Δ*T* increases from 18.3 K for Ni₁₁–EtOH to 23 K for Ni₉Fe_{0.5}, 25.7 K for Ni₇Fe₁, and 30.8 K for Ni₅Fe₂. The reference catalyst Ni₁₁–EtOH is the most stable

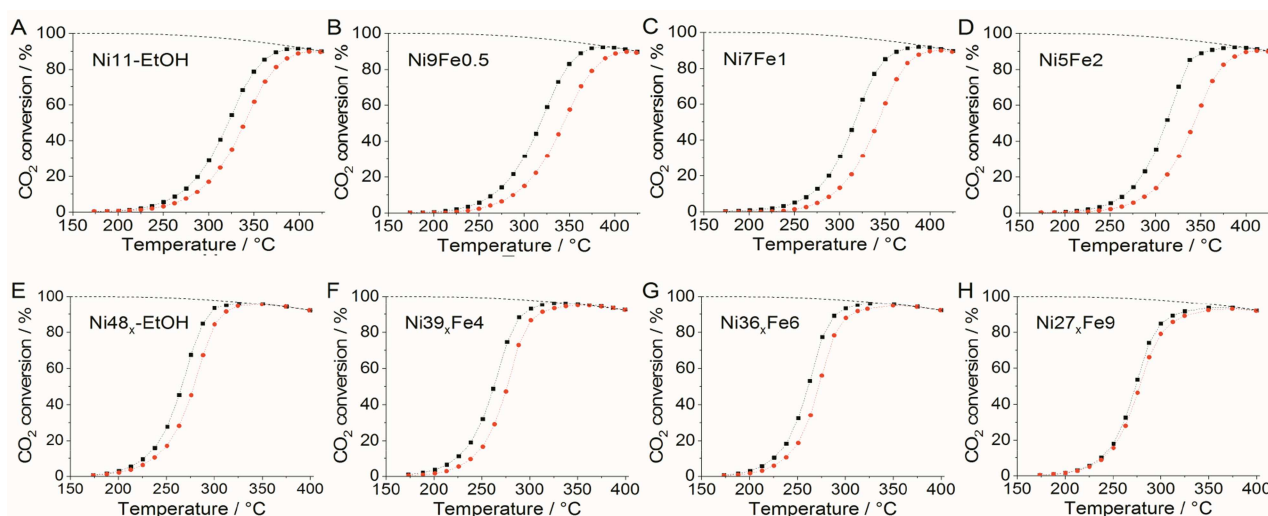


Figure 7. Temperature vs. CO₂ conversion plots for the Ni/Al₂O₃-based (A–D) and NiAlO_x-based (E–H) catalysts before (black squares) and after aging (red circles).

one, and the apparent stability decreases the higher the Fe loading.

The material properties after aging are listed in Table 2 (index 2: after aging). The CO₂ uptakes after aging are in the same order of magnitude and range from 119 μmol g_{cat}⁻¹ for Ni11–EtOH to 135 μmol g_{cat}⁻¹ for Ni7Fe1. The BET surface areas decrease to approx. 146 m² g_{cat}⁻¹ for all catalysts, while the total pore volumes stay approximately constant. The mean pore diameter increases to 10.9 nm for all catalysts.

As shown in Table 2, for all Ni/Al₂O₃-based catalysts, the Ni surface area decreases significantly during aging. The decrease amounts to 75 % for Ni11–EtOH and Ni9Fe0.5, 70 % for Ni7Fe1, and 60 % for Ni5Fe2. At the same time, evaluation of the XRD patterns after reduction reveals that the bulk composition of the (γFe,Ni) particles is altered during aging, leading to a slightly higher degree of alloying. The Ni/Fe ratio for these samples after aging is closer to the bulk Ni/Fe composition shown in Table 1. For Ni9Fe0.5, the alloy contains 4.5 wt.% Fe (previously 2.5 wt.%), for Ni7Fe1 6 wt.% (previously 4 wt.%), while it increases from 8 wt.% to 10.5 % for Ni5Fe2. The activation energies stay approximately constant; one could, however, suspect a small decrease at high Fe loadings. By a slightly higher degree of alloying, the surface concentration of the Fe-modified active sites might decrease (extent increasing with rising Fe loading), effectively leading to a decrease of the activity after aging, opposite to the trend in initial activity of the Fe-doped Ni/Al₂O₃-based catalysts.

The catalysts derived from the precipitated NiAlO_x catalysts (cf. Figure 7E–H) feature a significantly different behavior. The differences of the characteristic temperatures necessary for 50 % CO₂ conversion before and after aging amount to 12.6 K for Ni48_x–EtOH, 13.9 K for Ni39_xFe4, 11.0 K for Ni36_xFe6 and 4.4 K for Ni27_xFe9.

Similar to the Ni/Al₂O₃ based catalyst, the properties of the oxidic phase, BET surface area (approx. 125 m² g_{cat}⁻¹) and the total CO₂ uptake (approx. 125 m² g_{cat}⁻¹) decrease to the same values for all catalysts. The loss of Ni surface area ascribed to sintering can be calculated to be 56 % for Ni48_x–EtOH and Ni39_xFe4, 53 % for Ni36_xFe6, and only 24 % for Ni27_xFe9. The change in Ni surface area can be ascribed to two different effects: first, particle sintering may occur, as evident from the increase of the (γFe,Ni) crystallite size shown in Table 2, but also to a redistribution of the Fe centers on the metal surface, blocking or releasing H₂ adsorption sites on Ni. The bulk composition of the (γFe,Ni) particles undergoes significant changes during aging: for the Fe-containing NiAlO_x-based catalysts, the Ni/Fe ratios within the bulk alloy decreases. XRD analysis suggests that after the aging treatment the bulk of the (γFe,Ni) alloy particles contains 6.5 wt.% Fe in Ni39_xFe4 (previously 11 wt.%), 9 wt.% Fe in Ni36_xFe6 (previously 15.5 wt.%), and 11 wt.% Fe in Ni27_xFe9 (previously 21 wt.%), which can be interpreted as partial de-alloying of the metal particles.^[41]

To confirm the effect of the aging treatment on the composition of the metal particles, FMR was exemplarily carried out on the aged Ni27_xFe9 catalyst. The aging procedure led to clear changes in the ferromagnetic characteristics, reflected in

particular by a strong decrease in anisotropy (ΔB_{pp}) and Δg , of the main component, while a remaining background indicates residual Ni–Fe alloyed particles. The ferromagnetic contribution of iron is clearly reduced indicating de-alloying and possibly partial oxidation of Fe. Due to the complex interactions of metal particle sintering (cf. Table 2), particle composition, as well as possible changes of metal particle shape and particle stabilization effects on the oxidic phase over aging, however, conclusive statements or interpretations are not possible at the current state but are part of an ongoing study.

In concordance to the change in the alloy bulk composition over aging, differences in the apparent activation energies can be observed. While the apparent activation energy is constant for Ni48_x–EtOH and Ni39_xFe4, where the influence of Fe, in accordance to studies using co-precipitated Ni–Fe–Al catalysts,^[10a] might be too low, it increases by 4.1 kJ mol⁻¹ for Ni36_xFe6 and 7.4 kJ mol⁻¹ for Ni27_xFe9 over the aging treatment. These drastic changes once more indicate the presence of a compensation effect, caused by the change in the concentrations of exposed Fe sites due to dynamic variation of the (γFe,Ni) bulk composition under aging conditions. At the same time, the segregation process may lead to (a) generation of new active sites and (b) a decrease in the sintering rate of the Ni sites, resulting in an improved apparent catalyst stability.

A decisive statement on the exact composition of the active sites and the role of possible Fe²⁺ formation^[41] during the segregation process, however, cannot be made. Detailed time-resolved studies on catalyst activity as a function of aging time, coupled with detailed material characterization under inert conditions to further resolve structure-activity relationships are planned in an ongoing study using an industrially more relevant co-precipitated Ni–Fe–Al catalyst and might contribute to shine some light on these questions. With respect to this, we would like to note that the selectivities towards CH₄ or any of the by-products remained merely unchanged over aging, which is an indicator that no isolated Fe clusters on the catalyst surface were formed caused by the (partial) segregation of Ni–Fe during aging (cf. Figure SI 8).

2.6.7. Effect of Catalyst Aging on (γFe,Ni) Nanoparticle Composition and Fe Surface Enrichment on the Catalytic Activity

It can be concluded that, depending on the nature of the oxidic phase, the composition of the (γFe,Ni) nanoparticles can undergo changes under harsh methanation conditions. These modifications influence the nature and the number of active sites, leading to (a) differences in catalyst activity and (b) changes of the (apparent) stability under methanation conditions. Within the investigated Ni/Fe range, a high surface concentration of exposed Fe atoms, either for the freshly activated catalyst or by (partial) segregation of a Ni–Fe alloy, leads to an increase of the catalytic activity of the material.

This increase in activity is accompanied by an increase in the apparent activation energy, caused by the modification of the active sites. In fact, for each state, a relation between the

apparent activation energy and the bulk (γ Fe,Ni) nanoparticle composition can be found, which is depicted in Figure 8. With increasing Fe content in (γ Fe,Ni), the apparent activation energy rises for both the Ni/Al₂O₃- and the NiAlO_x-based catalysts. The (partial) segregation of the Ni–Fe particles during aging of the NiAlO_x-based catalysts leads to an increase of Fe sites on the surface and consequently to an increase of the apparent activation energy.

3. Conclusions

The redox surface reaction was successfully applied to selectively dope metallic Ni centers with Fe on a classical supported Ni/Al₂O₃ catalyst prepared by deposition-precipitation and a co-precipitated NiAlO_x catalyst. Activity and (apparent) catalyst stability were found to strongly depend on the surface concentration of Fe species on alloyed (γ Fe,Ni) nanoparticles formed after catalyst activation.

For the Ni/Al₂O₃-derived catalysts an increase of the catalytic activity with increasing Fe loading was found, but aging revealed a decrease of the (apparent) stability under methanation condition, possibly caused by a slightly deeper degree of alloying after aging. For the NiAlO_x-derived catalysts, in contrast, a substantial enhancement of the apparent thermal stability upon an aging treatment with increasing Fe loading was found, linked to the (partial) segregation of the previously alloyed Ni–Fe particles. For all catalysts containing Fe in considerable amounts (Ni/Fe approx. 6), a distinct compensation effect regarding the apparent activation energy was observed, strongly dependent on the surface concentration of Fe and most likely caused by the simultaneous occurrence of the methanation reactions over different active sites.

Further studies will focus on the time resolution of the deactivation behavior and modification of the aging conditions to decouple sintering and de-alloying effects. Material charac-

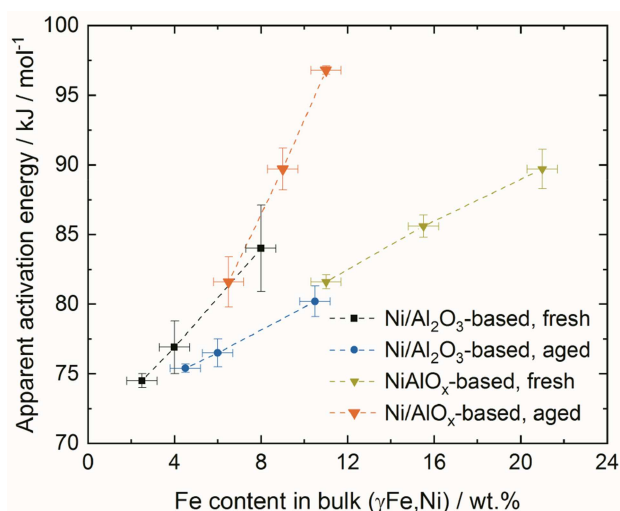


Figure 8. Trend of the apparent activation energy with (γ Fe,Ni) bulk composition. Dashed lines are only a guide to the eye.

terization studies under inert conditions at different states of deactivation may contribute to further elucidate the structure of the active sites on the (partly) deactivated Fe-promoted NiAlO_x catalysts.

Besides the surface redox reaction technique, also organo-metallic approaches are currently under investigation to allow to draw a comprehensive picture of the deactivation behavior of Fe-promoted Ni–Al catalysts.

Experimental Section

Preparation of Template Catalysts

The Ni/Al₂O₃ template catalyst was prepared by deposition-precipitation. 200 ml of a 0.02 M aqueous solution of Ni(NO₃)₂·6 H₂O (*p.a.*, Merck®) and of 1.3 M ammonia were added to 2.0 g Al₂O₃ (Sasol) in an open 500 ml Erlenmeyer flask with baffles. The suspension was mixed on a rotary platform shaker (Heidolph) with 150 rpm at room temperature for 48 h. The suspension was decanted and the solid was washed with DI water two times. After drying at room temperature for 18 h, the catalyst precursor was calcined at 450 °C for 3 h with a heating rate of 5 Kmin⁻¹. For activation, the Ni/Al₂O₃ template catalyst was heated from room temperature to 500 °C (at a linear heating rate of 2 K/min) in 50% H₂ in Ar and held there for one hour, before switching to a flow of 100% H₂ for another hour.

The NiAlO_x template catalyst was prepared by co-precipitation at a constant pH of 9. 120 ml of 1 M aqueous solutions of Ni(NO₃)₂·6 H₂O (*p.a.*, Merck®) and Al(NO₃)₃·9 H₂O (*p.a.*, Sigma-Aldrich®) were mixed and dropwise added to a 3 L double-walled glass vessel containing 1 L of bi-distilled water stirred at 150 rpm with a volumetric flow rate of 2.5 mlmin⁻¹. Two flow breakers were positioned in the vessel for secondary mixing. The temperature was pre-adjusted to 30 °C and kept constant during the synthesis by a thermostat, the pH was pre-adjusted to 9 by adding a 0.5 M mixture of 1 M solutions of Na₂CO₃ (Sigma-Aldrich®) and NaOH (Merck®). An Alkaline Titrimo Plus (Schott) was used to keep the pH constant at 9 ± 0.1 by adding the precipitation agent throughout the synthesis. The suspension was aged for 18 h in the mother liquor at pH 9 and 30 °C while further stirring. Afterwards, the suspension was vacuum-filtered and the filter cake was washed until the conductivity of the filtrate was similar to DI water. The filter cake was dried at 80 °C for 18 h.

The catalysts were calcined in flowing synthetic air at 450 °C for 6 h with a linear heating rate of 5 Kmin⁻¹. The catalyst powder was pelletized with a pressure of 450 Ncm⁻², ground and sieved to obtain a particle fraction of 150 to 200 μm. Detrimental effects on the porosity and the surface area of the catalysts at this pelletizing pressure were experimentally ruled out. The NiAlO_x template catalyst was reduced in H₂ at 500 °C for 5 h with a linear heating rate of 2 Kmin⁻¹.

Doping of the Template Catalysts with Fe

For both template catalysts, three SRR-modified catalysts were synthesized. For doping by means of the surface redox reaction technique, the activated catalyst was evacuated at 10⁻⁶ mbar at the reduction temperature for 1 h to free the Ni sites from H_{ads} species and cooled down to room temperature at 10⁻⁶ mbar.

Fe(NO₃)₃·9 H₂O (*p.a.*, Merck®) was dissolved in degassed and dried ethanol (*p.a.*, Merck®) before the solution was added to the

activated catalyst under Ar (purity 5.0) atmosphere. The synthesis parameters are listed in Table 3. The suspension was stirred at 300 rpm for 10 min. After filtration under Ar atmosphere, the catalyst was washed five times with degassed DI water. The catalyst was then vacuum-degassed at room temperature for 1 h, at 80 °C for 1 h and then at 250 °C for another 3 h.

The template catalysts were subjected to the same procedure without Fe being added, (labelled –EtOH) for better comparison. The so modified catalysts Ni11–EtOH and Ni48_x–EtOH serve as the benchmark catalysts throughout the studies. Catalyst testing and material characterization was carried out on the SRR-modified catalysts as well as their benchmark catalysts, respectively. An impact of EtOH on the physiochemical, morphologic and catalytic properties of the Ni–Al catalysts has been excluded by blank experiments.

Catalyst Testing Procedure

Catalyst testing was carried out in a setup described in a previous work.^[2c] 50 mg of catalyst in the particle size fraction from 150 to 200 μm were thoroughly mixed with 450 mg purified SiC (ESK) and placed in the isothermal zone of a 4 mm diameter glass-lined tube reactor. The absence of heat and mass transfer limitations for this specific particle size range under the chosen conditions had been excluded beforehand, both experimentally and by evaluating heat and mass transport criteria.^[2c,42] The axial position of the catalyst bed was fixed by 4 mm quartz wool plugs. To track bed temperature during reaction, a thermocouple was placed at the end of the diluted catalyst bed. The catalysts were *in situ* activated in H₂ ($Q = 60 \text{ NL g}_{\text{cat}}^{-1} \text{ h}^{-1}$) by heating to 500 °C with a linear heating rate of 2 K min⁻¹ and holding this temperature for 5 h. Initially, the catalyst was subjected to methanation conditions at 8 bar and 250 °C at 150 NL g_{cat}⁻¹ h⁻¹ (H₂/CO₂/Ar = 4/1/5) for 2 h. After this start-up phase, the temperature was varied stepwise from 175 °C to 500 °C at 8 bar to resolve data on the activity of the catalyst in the form of its CO₂ conversion versus temperature characteristics (labelled S1). In the following, the catalyst was subjected to an aging treatment at 500 °C and 8 bar for a duration of 32 h. After this artificial aging treatment, a second temperature variation cycle (S2) was carried out in order to resolve data indicating the apparent thermal stability of the catalyst under reaction conditions. The temperature program is shown in Figure SI 1. Data accuracy was checked in replicate experiments. To provide a clean surface prior the characterization of spent samples, the catalyst bed was heated up to 350 °C in Ar ($Q = 60 \text{ NL g}_{\text{cat}}^{-1} \text{ h}^{-1}$) for 1 h. Furthermore, after cool-down, the sample was removed from the setup under inert atmosphere and vacuum-degassed at 350 °C for 1 h.

The activation energies for CH₄ formation before and after aging were determined under differential conditions with the CO₂ conversion ranging from 2% to 10% by evaluating the slope of the logarithmic CH₄ formation rate plotted against 1/T. In advance, it was checked that the reaction orders of H₂ and CO₂ do not change in this regime. Experimental errors were calculated by Gaussian error propagation. The calculated and reported errors were higher than the errors observed in replicate experiments.

The purity of all gasses (Westfalen) was 5.0. The gas flow exiting the backpressure regulator was diluted with Ar in a ratio of 1/8. All tubing was heated to prevent water from condensation. An Emerson MTL-4 gas process analyzer was used for online tracking of the molar gas composition (CO₂, CO, H₂O, CH₄, and H₂). For each measurement point, the parameters were kept constant for 45 min. Steady-state conditions were reached after 20 min. The actual product gas composition was averaged over 150 s (300 data points). Byproduct analysis was performed on a Perkin Elmer Clarus

580 gas chromatograph equipped with two columns and FID detectors. C, H, and O balances were closed by ±3%. Conversions *X* and yields *Y* were calculated according to Equations (1) to (3), taking volume contraction into account according to Equation (4).

$$X(j) = \frac{\dot{n}_{\text{in}}(j) - \dot{n}_{\text{out}}(j)}{\dot{n}_{\text{in}}(j)} = \frac{X_{\text{PGA,in}}(j) \cdot (\dot{V}_{\text{in}} + \dot{V}_{\text{dil}}) - X_{\text{PGA,out}}(j) \cdot (\dot{V}_{\text{out}} + \dot{V}_{\text{dil}})}{X_{\text{PGA,in}}(j) \cdot (\dot{V}_{\text{in}} + \dot{V}_{\text{dil}})}, \quad (1)$$

$$j = \text{CO}_2, \text{H}_2$$

$$Y(i) = \frac{X_{\text{PGA,out}}(i) \cdot (\dot{V}_{\text{out}} + \dot{V}_{\text{dil}})}{X_{\text{PGA,in}}(\text{CO}_2) \cdot (\dot{V}_{\text{in}} + \dot{V}_{\text{dil}})}, \quad i = \text{CH}_4, \text{CO} \quad (2)$$

$$Y(\text{H}_2\text{O}) = 2 \cdot \frac{X_{\text{PGA,out}}(\text{H}_2\text{O}) \cdot (\dot{V}_{\text{out}} + \dot{V}_{\text{dil}})}{X_{\text{PGA,in}}(\text{H}_2) \cdot (\dot{V}_{\text{in}} + \dot{V}_{\text{dil}})} \quad (3)$$

$$\dot{V}_{\text{out}} = \frac{\dot{V}_{\text{in}} \cdot (1 - 2 \cdot x(\text{CO}_2)_{\text{in}}) + 2 \cdot \dot{V}_{\text{dil}} (x(\text{CO}_2)_{\text{out}} - x(\text{CO}_2)_{\text{in}})}{1 - 2 \cdot x(\text{CO}_2)_{\text{out}}} \quad (4)$$

$$S(k) = \frac{Y(k)}{X(\text{CO}_2)}, \quad k = \text{C}_x\text{H}_y, \text{CO} \quad (5)$$

Yields of the hydrocarbon byproducts were calculated from the FID response corrected by the sensitivity factors.^[43] Selectivities were calculated according to Equation (5). Enthalpy and entropy data for the calculation of equilibrium data were determined from the Shomate equation on the basis of data provided by the NIST Chemical WebBook. The calculation itself was carried out by the Δ*G* minimization method.

Elemental Analysis

Elemental analysis was carried out via inductively coupled plasma-optical emission spectroscopy (ICP-OES) on an Agilent 700. For sample preparation, approximately 50 mg of the catalyst were dissolved in 50 ml of 1 M H₃PO₄ by sonication for 2 h at 60 °C. The samples were cooled down and diluted in a ratio of 1/10 with bi-distilled water. The solutions were filtered using 0.45 μm syringe filters (Pall). The multi-element standard IV (Merck) was used to prepare metal standard solutions for 1, 10 and 50 ppm metal ion concentrations. Matrix interactions and metal signal interference were excluded. The wavelengths tracked for quantification were 230.299 nm (Ni), 396.152 nm (Al), 238.204 nm (Fe), and 568.263 nm (Na). All data were averaged over five measurements. The Na signal in all samples was below the detection limit (corresponding to a Na loading $w_{\text{Na}} < 10^{-3}$ wt.%), meaning that Na poisoning by the co-precipitation agent can be excluded.

X-ray Powder Diffraction Analysis

Ambient X-ray powder diffraction (XRD) was carried out on a Philips X'pert equipped with Cu–K_α radiation and a monochromator. The powders were scanned with 0.017° step⁻¹ and 83 steps min⁻¹. XRD on reduced and spent catalyst samples was carried out on a STOE Stadi P diffractometer using Cu–K_α radiation, a Ge(111) monochromator and a Dectris MYTHEN 1 K detector. Approximately 5 mg of catalyst was transferred into glass capillaries (outer diameter 0.5 mm) under Ar atmosphere. Diffractograms were taken in the range of 2θ = 5–90° with 0.015° step⁻¹ and a stepping rate of 45 steps min⁻¹. The mean particle diameters were calculated by line profiling (Pseudo Voigt function) using Highscore 3.0d, evaluating

the reflex caused by X-ray diffraction on the (020) plane at $2\theta = 51.5\text{--}51.8^\circ$ of Ni or (γ -Fe,Ni) crystallites, respectively. Nomenclature was taken from Swatzendruber et al.^[26] Estimation of the (γ -Fe,Ni) alloy particle composition was carried out by comparing the calculated cell parameter a of the fcc crystal lattice, determined from the reflection caused by the (020) plane at $2\theta = 51.5\text{--}51.8^\circ$, to tabulated values.^[26] From the XRD step-width, the absolute error in the molar Ni/Fe composition of the (γ -Fe,Ni) crystallites can be estimated to be ± 0.7 at. %.

Scanning Transmission Electron Microscopy/Energy Dispersive X-ray Spectroscopy

To evaluate the relative positions of Fe and Ni on the oxidized SRR-modified catalysts, energy dispersive X-ray (EDX) spectroscopy in scanning transmission electron microscopy (STEM) mode was carried out at 300 kV on a FEI Titan Themis microscope equipped with a Super-X EDX detector. 1 mg of catalyst powder was dispersed in bi-distilled H₂O and sonicated for 10 min. After sedimentation of the larger particles, 3 μ l of the suspension were dropped onto a carbon film coated copper grid. The droplet was removed after an adsorption time of 10 s using filter paper.

Temperature-Programmed Reduction

Temperature-programmed reduction (TPR) profiles were recorded by thermal gravimetric analysis/mass spectrometry (TG-MS) on a NETZSCH ST 409. The parameters were chosen in accordance to Malet and Caballero^[44] and Monti and Baiker.^[45] 50 mg of catalyst were heated in a flow of 60 ml min⁻¹ Ar to 350 °C with a linear heating rate of 5 K min⁻¹. After cooling down to room temperature, the sample was heated to 850 °C in 5% H₂ in Ar with a total volumetric flow rate of 70 ml min⁻¹ and a linear heating rate of 5 K min⁻¹. To gather the TPD patterns, the H₂O signal at $m/z = 18$ was evaluated. Data was smoothed using a Loess filter with a span of 0.03. For determination of the reduction temperatures the signals were deconvoluted by Gaussian peak fitting.

N₂ Physisorption

N₂ physisorption experiments on activated and spent catalyst samples were carried out at 77 K samples on a Quantachrome NOVAtouch. For the determination of the BET surface area, the p/p_0 range between 0.05 and 0.3 was taken for evaluation. For the catalysts derived from the precipitated Ni/Al₂O₃ catalyst, the total pore volume was taken from the data point at $p/p_0 = 0.995$. For the Al₂O₃-based catalysts, the pore size distribution was determined applying the BJH method on the adsorption branch since the samples exhibited type IV isotherms featuring a H₂ hysteresis. The N₂ physisorption characteristics of the samples derived from the co-precipitated template catalyst can be classified into type IV isotherms featuring a H₃ hysteresis, which is a hint for plate-like particles or slit-like pores. Therefore, the conventional theories on the pore volume and pore sizes determination cannot be applied.^[46] For this reason, reporting of the total pore volumes and the pore size distributions for the NiAlO_x-based catalyst is omitted.

H₂ and CO₂ Chemisorption

H₂ and CO₂ chemisorption experiments were conducted on an Autosorb 1 C (Quantachrome). For the pre-treatment, the fresh catalysts were activated in H₂ at 500 °C for 5 h (linear heating rate 2 K min⁻¹). Adsorption equilibration time was set 2 min (H₂) and 10 min (CO₂), respectively. A dissociative adsorption mechanism of

H₂ on Ni was applied for the calculation of the specific metal surface area.^[47] As generally accepted in literature,^[25,31] it was assumed that under the chosen conditions H₂ exclusively adsorbs on Ni and not on Fe. Furthermore, in preliminary studies it was ensured that the adsorption of CO₂ at the chosen conditions was not kinetically hindered on our samples.

Paramagnetic and Ferromagnetic Resonance Spectroscopy

Paramagnetic and ferromagnetic resonance (EPR/FMR) spectra of the activated catalysts were recorded on a JEOL JES-RE 2X at X-band frequency at temperatures between 113 and 473 K, a microwave frequency of 9.4 GHz, a microwave power < 0.2 mW, and a modulation frequency of 100 kHz. The microwave frequency was measured with a microwave frequency counter Advantest R5372. The catalyst samples were transferred into glass capillaries (diameter 0.5 mm) after activation (fresh catalyst samples) without contact to air. The integrated intensity was determined by double integration of the resonance signals of a weighed catalyst sample calibrated to a known standard (Mn²⁺/MgO). Conclusions on FMR data of the aged catalyst samples are difficult to interpret due to factors like particle size and shape^[27a] (owed to possibly different susceptibilities to sintering), possible adsorbates on the catalyst surface^[27c] as well as modified particle-support interactions^[27b] during aging, influencing ferromagnetic characteristics like magnetic intensity and anisotropy. Investigations on aged samples by FMR and their interpretation are part of an ongoing study.

Temperature-programmed Desorption of CO₂

CO₂-TPD was carried out in a setup described elsewhere.^[35] 50 mg of catalyst powder was reduced at 480 °C in 5% H₂ in He for 5 h (linear heating rate 2 K min⁻¹). After purging with He for 1 h, the catalyst bed was cooled down to 35 °C in He. The catalyst was treated with CO₂ for 30 min at 35 °C, before weakly adsorbed CO₂ was removed by purging with He for 30 min. The TPD was carried out from 35 to 480 °C with a linear heating rate of 6 K min⁻¹ using He (Westfalen, 6.0) carrier gas (100 ml min⁻¹). Due to unknown adsorption and desorption kinetics, fitting of the CO₂ desorption signal was omitted.

Acknowledgements

T. Burger and H. Augenstein acknowledge the support of the TUM Graduate School. The authors would like to thank Prof. T. Nilges, Prof. S. Günther, Stefan Ewald and Stefan Burger for fruitful discussions, Dr. C. Haeßner for recording the EPR/FMR spectra.

Conflict of Interest

The authors declare no conflict of interest.

Keywords: surface redox reaction · Ni–Fe segregation · CO₂ methanation · Fe promoter · co-precipitated NiAlO_x catalyst

[1] M. Sterner, Kassel University 2009.

[2] a) A. Erhan Aksoylu, Z. Ilseñonsan, *Appl. Catal. A* **1997**, *164*, 1–11; b) S. Abello, C. Berruoco, F. Gispert-Guirado, D. Montane, *Catal. Sci. Technol.* **2016**, *6*, 2305–2317; c) F. Koschany, D. Schlereth, O. Hinrichsen, *Appl.*

- Catal. B* **2016**, *181*, 504–516; d) T. Inui, M. Funabiki, M. Suehiro, T. Sezume, *J. Chem. Soc. Faraday Trans. 1* **1979**, *75*, 787–802.
- [3] C. H. Bartholomew, *Appl. Catal. A* **2001**, *212*, 17–60.
- [4] U. S. G. Survey, *Metal prices in the United States through 2010: U.S. Geological Survey Scientific Investigations report 2012–5188*, **2013**, p. 204.
- [5] a) P. Sabatier, J. B. Senderens, *C. R. Acad. Sci.* **1902**, *134*, 689–691; b) H. Habazaki, M. Yamasaki, B.-P. Zhang, A. Kawashima, S. Kohno, T. Takai, K. Hashimoto, *Appl. Catal. A* **1998**, *172*, 131–140; c) J. L. Falconer, A. E. Zagli, *J. Catal.* **1980**, *62*, 280–285; d) A. E. Zagli, J. L. Falconer, C. A. Keenan, *J. Catal.* **1979**, *56*, 453–467; e) C. Schild, A. Wokaun, R. A. Koeppl, A. Baiker, *J. Phys. Chem.* **1991**, *95*, 6341–6346.
- [6] F. Solymosi, A. Erdöhelyi, T. Bansagi, *J. Catal.* **1981**, *68*, 371–382.
- [7] A. Erdöhelyi, M. Pásztor, F. Solymosi, *J. Catal.* **1986**, *98*, 166–177.
- [8] G. Garbarino, P. Riani, L. Magistri, G. Busca, *Int. J. Hydrogen Energy* **2014**, *39*, 11557–11565.
- [9] F. Solymosi, A. Erdöhelyi, *J. Mol. Catal.* **1980**, *8*, 471–474.
- [10] a) T. Burger, F. Koschany, O. Thomys, K. Köhler, O. Hinrichsen, *Appl. Catal. A* **2018**, *558*, 44–54; b) B. Mutz, M. Belimov, W. Wang, P. Sprenger, M.-A. Serrer, D. Wang, P. Pfeifer, W. Kleist, J.-D. Grunwaldt, *ACS Catal.* **2017**, *6802–6814*; c) D. Pandey, G. Deo, *J. Mol. Catal. A* **2014**, *382*, 23–30; d) D. Pandey, G. Deo, *J. Ind. Eng. Chem.* **2016**, *33*, 99–107; e) S. Hwang, U. G. Hong, J. Lee, J. H. Baik, D. J. Koh, H. Lim, I. K. Song, *Catal. Lett.* **2012**, *142*, 860–868; f) C. Mebrahtu, F. Krebs, S. Perathoner, S. Abate, G. Centi, R. Palkovits, *Catal. Sci. Technol.* **2018**, *8*, 1016–1027.
- [11] B. Miao, S. S. K. Ma, X. Wang, H. Su, S. H. Chan, *Catal. Sci. Technol.* **2016**, *6*, 4048–4058.
- [12] a) A. Westermann, B. Azambre, M. C. Bacariza, I. Graça, M. F. Ribeiro, J. M. Lopes, C. Henriques, *Appl. Catal. B* **2015**, *174–175*, 120–125; b) P. A. U. Aldana, F. Ocampo, K. Kobl, B. Louis, F. Thibault-Starzyk, M. Daturi, P. Bazin, S. Thomas, A. C. Roger, *Catal. Today* **2013**, *215*, 201–207; c) Q. Pan, J. Peng, T. Sun, S. Wang, S. Wang, *Catal. Commun.* **2014**, *45*, 74–78.
- [13] a) S. Eckle, H.-G. Anfang, R. J. Behm, *J. Phys. Chem. C* **2011**, *115*, 1361–1367; b) S. Akamaru, T. Shimazaki, M. Kubo, T. Abe, *Appl. Catal. A* **2014**, *470*, 405–411.
- [14] a) T. Mori, H. Masuda, H. Imai, A. Miyamoto, S. Baba, Y. Murakami, *J. Phys. Chem.* **1982**, *86*, 2753–2760; b) M. P. Andersson, F. Abild-Pedersen, I. N. Remediakis, T. Bligaard, G. Jones, J. Engbæk, O. Lytken, S. Horch, J. H. Nielsen, J. Sehested, J. R. Rostrup-Nielsen, J. K. Nørskov, I. Chorkendorff, *J. Catal.* **2008**, *255*, 6–19; c) S. V. Ho, P. Harriott, *J. Catal.* **1980**, *64*, 272–283.
- [15] a) T. Bligaard, J. K. Nørskov, S. Dahl, J. Matthiesen, C. H. Christensen, J. Sehested, *J. Catal.* **2004**, *224*, 206–217; b) M. P. Andersson, T. Bligaard, A. Kustov, K. E. Larsen, J. Greeley, T. Johannessen, C. H. Christensen, J. K. Nørskov, *J. Catal.* **2006**, *239*, 501–506.
- [16] A. L. Kustov, A. M. Frey, K. E. Larsen, T. Johannessen, J. K. Nørskov, C. H. Christensen, *Appl. Catal. A* **2007**, *320*, 98–104.
- [17] T. Burger, F. Koschany, A. Wenng, O. Thomys, K. Köhler, O. Hinrichsen, *Catal. Sci. Technol.* **2018**, *8*, 5920–5932.
- [18] F. H. Meng, P. Z. Zhong, Z. Li, X. X. Cui, H. Y. Zheng, *J. Chem.* **2014**, *2014*, 1–7.
- [19] a) J. Gu, Y.-W. Zhang, F. Tao, *Chem. Soc. Rev.* **2012**, *41*, 8050–8065; b) G. Zhang, X. Liu, Y. Wang, C. Liu, S. Xing, *Chem. Eur. J.* **2017**, *23*, 5557–5564.
- [20] H. Li, Y. Xu, C. Gao, Y. Zhao, *Catal. Today* **2010**, *158*, 475–480.
- [21] E. C. Krüssink, L. L. van Reijen, J. R. Ross, *J. Chem. Soc. Faraday Trans. 1* **1981**, *77*, 649–663.
- [22] L. E. Alzamora, J. R. H. Ross, E. C. Krüssink, L. L. van Reijen, *J. Chem. Soc. Faraday Trans. 1* **1981**, *77*, 665–681.
- [23] E. C. Krüssink, E. B. M. Doesburg, L. L. van Reijen, L. E. Alzamora, S. Orr, J. R. H. Ross, G. van Veen, *Stud. Surf. Sci. Catal., Vol. Volume 3* (Eds.: P. G. P. J. B. Delmon, G. Poncelet), Elsevier, **1979**, pp. 143–157.
- [24] J. F. LePage, R. Schlögl, M. S. Wainwright, F. Schüth, K. Unger, E. I. Ko, H. Jacobsen, P. Kleinschmit, R. G. Menon, B. Delmon, K. Y. Lee, M. Misino, S. T. Oyama, *Handbook of Heterogeneous Catalysis*, Wiley-VCH Verlag GmbH, **2008**, pp. 49–138.
- [25] Z. Yu, D. Chen, M. Rønning, T. Vrålstad, E. Ochoa-Fernández, A. Holmen, *Appl. Catal. A* **2008**, *338*, 136–146.
- [26] L. J. Swartzendruber, V. P. Itkin, C. B. Alcock, *Phase diagrams of binary nickel alloys, Vol. 6* (Ed.: P. Nash), ASM International, Materials Park, Ohio, **1991**, pp. 110–132.
- [27] a) E. G. Derouane, A. Simoens, C. Colin, G. A. Martin, J. A. Dalmon, J. C. Védrine, *J. Catal.* **1978**, *52*, 50–58; b) E. G. Derouane, A. J. Simoens, J. C. Védrine, *Chem. Phys. Lett.* **1977**, *52*, 549–553; c) A. A. Andreev, P. W. Selwood, *J. Catal.* **1967**, *8*, 375–382.
- [28] A. M. Zhao, W. Y. Ying, H. T. Zhang, H. F. Ma, D. Y. Fang, *J. Nat. Gas Chem.* **2012**, *21*, 170–177.
- [29] K. Zhao, Z. Li, L. Bian, *Front. Chem.* **2016**, *10*, 273–280.
- [30] a) M. Gabrovska, R. Edreva-Kardjieva, D. Crişan, P. Tzvetkov, M. Shopska, I. Shtereva, *React. Kin. Mech. Catal.* **2012**, *105*, 79–99; b) J. Zhang, H. Xu, X. Jin, Q. Ge, W. Li, *Appl. Catal. A* **2005**, *290*, 87–96; c) B. Vos, E. Poels, A. Bliet, *J. Catal.* **2001**, *198*, 77–88.
- [31] H. J. Jung, M. A. Vannice, L. N. Mulay, R. M. Stanfield, W. N. Delgass, *J. Catal.* **1982**, *76*, 208–224.
- [32] H. Topsøe, N. Topsøe, H. Bohlbro, J. A. Dumesic, *Stud. Surf. Sci. Catal., Vol. 7* (Eds.: T. Seivama, K. Tanabe), Elsevier, **1981**, pp. 247–265.
- [33] M. Boudart, A. Delbouille, J. A. Dumesic, S. Khammouma, H. Topsøe, *J. Catal.* **1975**, *37*, 486–502.
- [34] X. Wang, M. Shen, L. Song, Y. Su, J. Wang, *Chem. Chem. Phys.* **2011**, *13*, 15589–15596.
- [35] S. Ewald, S. Standl, O. Hinrichsen, *Appl. Catal. A* **2018**, *549*, 93–101.
- [36] J. Sehested, K. E. Larsen, A. L. Kustov, A. M. Frey, T. Johannessen, T. Bligaard, M. P. Andersson, J. K. Nørskov, C. H. Christensen, *Top. Catal.* **2007**, *45*, 9–13.
- [37] E. Cremer, *Advances in Catalysis, Vol. 7* (Eds.: W. G. Frankenburg, V. I. Komarewsky, E. K. Rideal), Academic Press, **1955**, pp. 75–91.
- [38] a) H. Eyring, *Chem. Rev.* **1935**, *17*, 65–77; b) H. Eyring, *J. Chem. Phys.* **1935**, *3*, 107–115.
- [39] S. Ewald, M. Kolbeck, T. Kratky, M. Wolf, O. Hinrichsen, *Appl. Catal. A* **2019**, *570*, 376–386.
- [40] C. J. Wright, C. G. Windsor, D. C. Puxley, *J. Catal.* **1982**, *78*, 257–261.
- [41] S. M. Kim, P. M. Abdala, T. Margossian, D. Hosseini, L. Foppa, A. Armutlulu, W. van Beek, A. Comas-Vives, C. Copéret, C. Müller, *JACS* **2017**, *139*, 1937–1949.
- [42] a) J. B. Anderson, *Chem. Eng. Sci.* **1963**, *18*; b) D. E. Mears, *Ind. Eng. Chem. Process Des. Dev.* **1971**, *10*, 541–547; c) P. B. Weisz, C. D. Prater, *Adv. Catal., Vol. 6* (Eds.: W. G. Frankenburg, V. I. Komarewsky, E. K. Rideal), Academic Press, **1954**, pp. 143–196.
- [43] W. A. Dietz, *J. Chromatogr. Sci.* **1967**, *5*, 68–71.
- [44] P. Malet, A. Caballero, *J. Chem. Soc. Faraday Trans. 1* **1988**, *84*, 2369–2375.
- [45] D. A. M. Monti, A. Baiker, *J. Catal.* **1983**, *83*, 323–335.
- [46] K. S. Singh, J. Rouquerol, G. Bergeret, P. Gallezot, M. Vaarkamp, D. C. Koningsberger, A. K. Datye, J. W. Niemantsverdriet, T. Butz, G. Engelhardt, G. Mestl, H. Knözinger, H. Jobic, *Handbook of Heterogeneous Catalysis*.
- [47] C. H. Bartholomew, R. B. Pannell, *J. Catal.* **1980**, *65*, 390–401.

Manuscript received: July 24, 2019

Revised manuscript received: October 9, 2019

Accepted manuscript online: October 9, 2019

Version of record online: November 26, 2019